OPERATIONAL UNDERWATER NOISE FROM A MONOPILE-SUPPORTED OFFSHORE WIND TURBINE: A VIBROACOUSTIC ANALYSIS

Raúl Sanz-Ramírez[1], Martín de Frutos[1], Esteban Ferrer[1]

[1] *Department of Applied Mathematics to Aerospace Engineering, Universidad Politécnica de Madrid, Spain*

Abstract

Anthropogenic underwater noise from offshore wind turbines is an increasingly relevant environmental concern, particularly for fixed-bottom installations such as monopile foundations. This work presents a physics-based framework for predicting operational structure-borne underwater noise from a monopile-supported offshore wind turbine.

The methodology combines time-domain aero-hydro-servo-elastic simulations performed with OpenFAST with a frequency-domain acoustic model based on equivalent dipole sources and analytical Green's functions. Free-surface and seabed reflections are incorporated through the method of images. To account for high-frequency vibrations not resolved by the aeroelastic solver, a synthetic drivetrain excitation model is introduced.

The results show two distinct radiation regimes. At low frequencies, the acoustic field is governed by global bending modes of the tower–monopile assembly, producing a dipolar directivity pattern aligned with the turbine axis. At mid- and high frequencies, drivetrain-induced vibrations dominate the response and generate a more axisymmetric radiation pattern. The shallow-water environment further modifies propagation, promoting cylindrical-like spreading and reduced vertical variability of the acoustic field.

The proposed framework provides a computationally efficient tool for estimating operational underwater noise during the design phase of offshore wind turbines and may support future environmental assessment and monitoring strategies.

Keywords: *Offshore Wind turbine, Vibro-Acoustics, Underwater noise, Structure-borne noise, Monopile foundations*

Corresponding author: *raul.sanz.ramirez@upm.es.*

1. Introduction

Anthropogenic underwater noise is an increasing environmental concern, particularly the continuous low-frequency noise from offshore wind turbines during operation, which is less studied than impulsive sources such as pile driving [1], [2], [3]. Among the fixed bottom support structures, the monopile foundation is the most widely deployed, making its dynamic and acoustic behaviour under operational conditions especially relevant [4].

Operational noise originates from two main pathways: airborne aeroacoustic noise at the rotor and structure-borne vibroacoustic radiation through the support structure. Recent work [5] has shown that aeroacoustic energy can propagate into the water column through air–water coupling, but this mechanism is distinct from structure-borne transmission. The present study focuses on vibroacoustic noise, which arises from fluctuating aerodynamic thrust, drivetrain excitation, and hydrodynamic loading inducing vibrations that propagate along the tower and monopile and radiate into the water [3], [4].

Predictive physics-based tools for underwater noise are still limited, with most environmental assessments relying on post hoc measurements. A validated framework would allow noise quantification during the design phase and support future regulatory standards. Therefore, this study develops a predictive vibroacoustic framework for a monopile-supported offshore wind turbine, focusing on structure-borne noise under rated operating conditions. The main contributions are: (i) an integrated modelling framework coupling aeroelastic loading, structural dynamics, fluid–structure interaction, and acoustic propagation; (ii) definition of measurable acoustic descriptors for consistent characterisation of radiated sound; and (iii) identification of the physical mechanisms governing the operational underwater noise signature of bottom-fixed turbines.

2. Methodology

The study couples time-domain aero-hydro-servo-elastic simulations (OpenFAST) of a 10 MW monopile-supported turbine with a frequency-domain acoustic model based on equivalent dipole sources and the method of images.

2.1. Turbine and Support Structure

The reference turbine is the DTU 10 MW [6], whose main characteristics are given in Table 1. Simulations are performed at a steady uniform inflow of 11.4 m/s (9.6 rpm, $\lambda = 6$) to ensure stationary structural response.

Characteristic	DTU 10 MW
Hub height [m]	119.0
Rotor diameter [m]	178.4
Nominal wind velocity [m/s]	11.4
Rotor angular velocity [rpm]	9.6
Blade tip velocity [m/s]	90.0
Blade Pitch [deg.]	10.5

Table 1: Geometrical and operational (rated) conditions of DTU 10 MW [6].

2.2. Structural Dynamics

OpenFAST [7] solves the coupled equations of motion in the time domain. The tower and blades are modelled with beam elements (`ElastoDyn`), while the monopile is represented by a first-order finite element formulation (Timoshenko beams) in `SubDyn` [8]. Hydrodynamic loads (`HydroDyn`) include wave excitation, added mass, radiation damping, and hydrostatic restoring. Only the 25 submerged nodes ($z < 0$) are retained as acoustic sources.

The dominant eigenfrequencies lie below 5 Hz (global bending). Higher-frequency drivetrain-induced vibrations [9], [10], [11], [12] are introduced via a synthetic excitation at the hub. A mesh convergence study (Fig. 1) confirmed that the 25-node discretisation is sufficient.

Time-domain simulations run for 130 s; the first 30 s are discarded. With $\Delta t = 5 \times 10^{-4}$ s ($f_s = 2000$ Hz, Nyquist 1000 Hz) and $T = 100$ s, the frequency resolution is 0.01 Hz. Nodal accelerations are windowed (Hann), mean-subtracted, and Fourier-transformed to obtain complex spectra, which are then multiplied by the effective nodal mass to yield dipole forces.

2.3. Acoustic Model

Assuming small-amplitude vibrations in a quiescent fluid, structural vibrations are modelled as localised oscillatory body forces acting on the surrounding fluid. Under the linear acoustic approximation, higher-order nonlinear and quadrupole contributions are negligible [13], and the dominant radiation mechanism is dipolar, associated with fluctuating inertial forces without net mass injection. Each submerged node n is treated as a point dipole whose strength is obtained from the local acceleration $\mathbf{a}_n$ and a frequency-dependent radiation

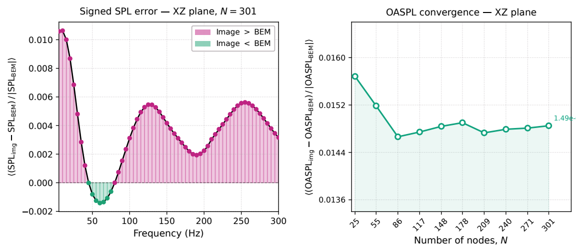

Figure 1: Validation of the proposed acoustic methodology against a three-dimensional Boundary Element Method (BEM) solution for a submerged monopile in free space. Left: mean signed relative SPL error over the evaluation plane as a function of frequency. Right: convergence of the maximum relative error with increasing number of equivalent dipole nodes.

correction $\gamma(\omega, R_n)$ [14]:

$$\mathbf{f}_n(\omega) = \gamma(\omega, R_n)\, m_{\mathrm{struct},n}\, \mathbf{a}_n(\omega), \qquad (1)$$

with $m_{\mathrm{struct},n} = \rho_{\mathrm{mat}} A_n \Delta z_n$. The factor γ accounts for the transition from added-mass dominance at low frequencies to bare dipole radiation at high frequencies. The total acoustic pressure is then obtained by linear superposition of all N_d dipole contributions [15]:

$$\tilde{p}(\mathbf{x}, \omega) = \sum_{n=1}^{N_d} \frac{1}{4\pi r_n} \left(\frac{1}{r_n} - i k_0 \right) \left(\tilde{\mathbf{f}}_n(\omega) \cdot \hat{\mathbf{r}}_n \right) e^{i k_0 r_n}, \qquad (2)$$

where $k_0 = \omega / c_0$, $r_n = |\mathbf{x} - \mathbf{x}_n|$, and $\hat{\mathbf{r}}_n$ is the unit vector from the n-th source to the observer. Validation against a full BEM solution (Fig. 1) shows errors below 1%.

2.4. Boundary Conditions: Method of Images

The free surface ($z = 0$) is treated as a pressure-release boundary ($\tilde{p} = 0$) and the seabed ($z = -H$) as a partially reflecting boundary with a constant reflection coefficient $R_b = 0.5$ [16]. Image dipoles are introduced by successive mirroring across both boundaries, yielding an infinite series. A convergence study showed that $N = 30$ images per side reduce the relative error below 10^{-13}. All subsequent results use this truncation.

2.5. Drivetrain Excitation Model

OpenFAST does not resolve high-frequency internal drivetrain dynamics. Therefore, a synthetic excitation force is applied at the generator location, representing shaft harmonics and gear-mesh frequencies of a medium-speed 10 MW gearbox [17]. Amplitudes follow an exponential decay with harmonic order and are weighted by stage, consistent with typical torsional energy distributions [18], [19], [20]. Modal amplification is included via a set of lightly damped torsional modes ($\zeta = 2\%$) [21], and a narrow Gaussian broadening is applied to mesh components to mimic realistic spectral spreading. The resulting signal is scaled to match the RMS level reported by Wang et al. [22].

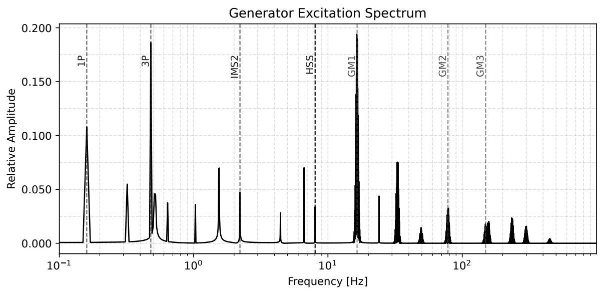

Figure 2: Frequency spectrum of the reconstructed generator excitation signal (normalized to unit RMS). Labels: 1P (rotor frequency), 3P (blade-passing harmonic), LSS (low-speed shaft), IMS (intermediate-speed shaft), HSS (high-speed shaft), GM1–GM3 (gear-mesh frequencies of stages 1–3).

3. Results

The acoustic field is characterised across a range of frequencies, spatial configurations, and receiver distances, enabling a thorough characterisation of the structure-borne underwater noise signature under rated operating conditions.

3.1. Radiated Acoustic Spectra

The narrowband sound pressure level (SPL) is used as the primary descriptor of tonal and broadband content. For each frequency, the complex pressure amplitude is converted to an RMS value and expressed in dB re 1 μPa:

$$\mathrm{SPL}(f) = 20\log_{10}\left(\frac{|p(f)|}{\sqrt{2}\,p_{\mathrm{ref}}}\right), \qquad p_{\mathrm{ref}} = 1\,\mu\mathrm{Pa}. \quad (3)$$

A frequency-dependent absorption correction is additionally applied following the Thorp model [23], using the straight-line source–receiver distance as a conservative lower bound of the actual propagation path, so that high-frequency attenuation is not overestimated.
Fig. 3 shows the narrowband SPL at a near-field receiver (10 m downstream, mid-depth). Discrete tonal peaks are clearly identifiable, corresponding to rotor harmonics and global bending modes of the tower–monopile assembly at low frequencies, and to drivetrain shaft and gear-mesh harmonics at higher frequencies, consistent with the excitation spectrum of Fig. 2.
Fig. 4 presents the mid- to high-frequency spectrum in 1/3-octave bands [24], with hearing thresholds for representative marine species superimposed cite-Tougaard2021,NMFS2024,Erbe2016. The emitted noise overlaps with the functional auditory ranges of several marine groups across a broad frequency interval, indicating that the signal is in principle detectable at close range. However, audibility does not imply physiological impact, as noise-induced effects depend on exposure levels and duration rather than threshold exceedance alone [25], and rapid geometric spreading significantly limits the biologically relevant

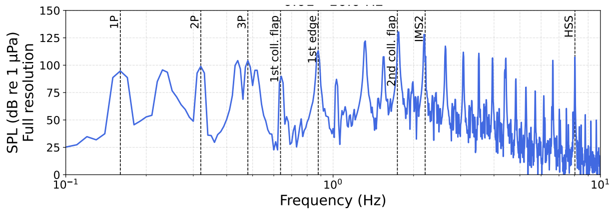

Figure 3: Narrowband Sound Pressure Level spectra in the low-frequency range (0–10 Hz) evaluated at a receiver located 10 m from the turbine at $z = -15$ m. Dashed lines indicate blade passing harmonics (1P, 2P and 3P), characteristic drivetrain frequencies IMS and HSS (intermediate- and high-speed shaft) and structural modal frequencies (first collective flap, first edge and second collective flap modes) reported in [6].

spatial extent.

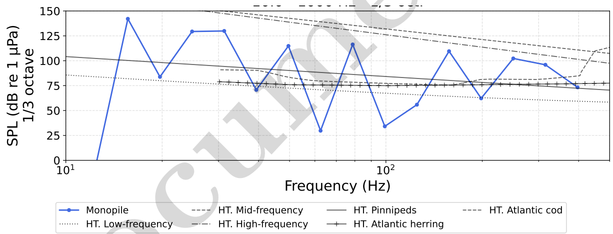

Figure 4: One-third octave band Sound Pressure Level spectra (10–1000 Hz) evaluated at a receiver located 10 m from the turbine at $z = -15$ m compared with marine fauna hearing thresholds from [26], [27], [28].

3.2. Directivity Patterns

The OASPL is obtained by energetic summation of the narrowband SPL over a prescribed frequency band:

$$\mathrm{OASPL}_{[f_1,f_2]} = 10\log_{10}\left(\sum_{f=f_1}^{f_2} 10^{\mathrm{SPL}(f)/10}\right). \quad (4)$$

Fig. 5 shows the polar distribution of OASPL at $r = 500$ m and $z = -15$ m for three frequency bands. At low frequencies, the radiated field exhibits a clear dipolar pattern aligned with the streamwise direction, governed by the dominant fore–aft global bending mode excited by periodic aerodynamic thrust. At higher frequencies, the directivity becomes substantially more axisymmetric, with only a slight preference for radiation perpendicular to the turbine axis, consistent with drivetrain-induced excitation: since shaft and gear-mesh loads are torsional and rotational in nature rather than associated with a single translational mode, the resulting radiation is more spatially distributed [18], [29].
The planar OASPL distributions in Fig. 6 confirm these observations. In the vertical plane ($y = 0$), energy spreads predominantly perpendicular to the turbine axis, consistent with quasi-2D propagation when the acoustic wavelength is comparable to or larger than the water column height. In the horizontal

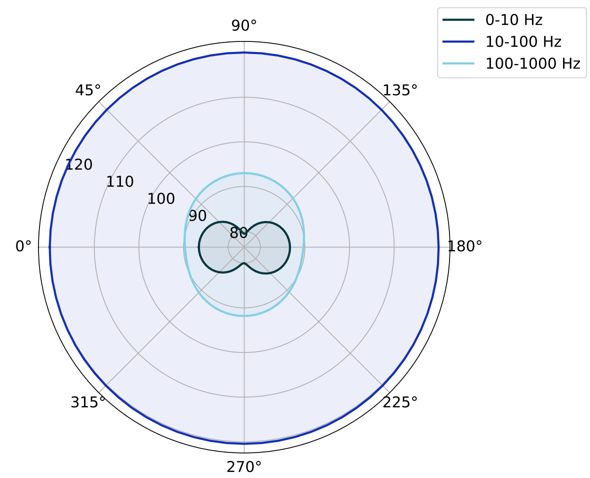

Figure 5: Polar distribution of OASPL at a radius of 500 m and depth z = -15 m, separated by frequency bands (0–10 Hz blue, 10–100 Hz orange, 100–1000 Hz green)

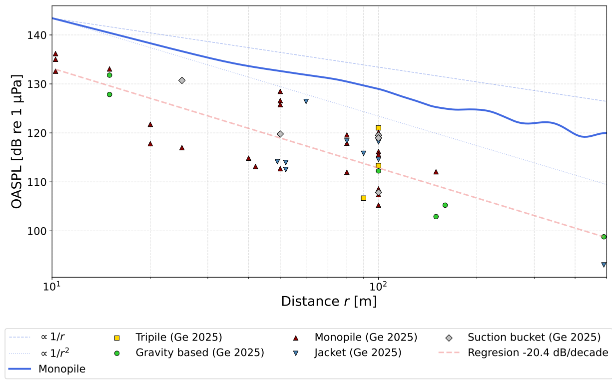

Figure 7: OASPL decay with distance along the downstream direction (y = 0, z = -15 m). Reference slopes corresponding to cylindrical ($1/r$) and spherical ($1/r^2$) spreading are shown. A regression fitted to the compiled dataset of offshore wind turbine measurements is also included, yielding a decay rate of -20.4 dB per decade.

plane ($z = -15$ m), the field is nearly homogeneous azimuthally, decaying regularly with distance from the source.

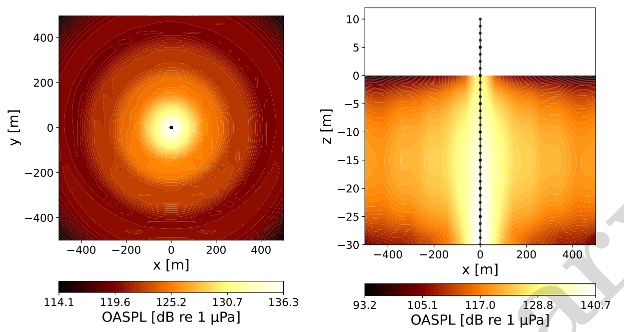

Figure 6: OASPL in the horizontal plane $z = -15$ m (left) and in the vertical streamwise plane $y = 0$ m (right).

3.3. Distance Decay Analysis

Fig. 7 shows the OASPL decay along the downstream axis ($y = 0$, $z = -15$ m), with receiver positions logarithmically spaced between 10 m and 500 m. Reference slopes for cylindrical (-10 dB/decade, $|p| \propto 1/\sqrt{r}$) and spherical (-20 dB/decade, $|p| \propto 1/r$) spreading are included for reference.

In the immediate vicinity of the structure (below ~ 50 m), the decay is somewhat steeper, reflecting near-field effects. Beyond this distance, the OASPL decreases at a rate close to 10 dB per decade, consistent with cylindrical spreading. Two mechanisms explain this behaviour. First, shallow-water confinement ($H = 30$ m) restricts vertical propagation when the acoustic wavelength is comparable to or larger than the water depth ($kH \lesssim 1$), channelling energy horizontally in a quasi-2D waveguide regime. Second, the vertically distributed submerged sources of the monopile resemble a finite line radiator, which inherently promotes $1/\sqrt{r}$-type attenuation in the horizontal plane.

Field measurements from [30] for a variety of offshore wind turbines are also shown for context. Many exhibit steeper decay rates, closer to spherical spreading, as they correspond to floating configurations in deeper water with considerably different environmental conditions. The measured absolute levels are also generally lower, which is consistent with the fact that most turbines in the compiled dataset are rated below 5 MW — significantly smaller than the 10 MW reference turbine considered here — and were measured under a wide range of operational and ocean conditions. The predicted decay trend is physically consistent and lies within the observed range, despite the simplified seabed representation (constant $R_b = 0.5$), static free-surface condition, and conservative straight-ray absorption correction, all of which may lead to a slight overestimation of absolute levels at longer ranges.

4. Discussion

The underwater acoustic signature of the monopile is governed by the interplay between structural dynamics and environmental confinement. At low frequencies, global bending modes of the tower–monopile assembly, excited by periodic aerodynamic thrust, produce a dipolar directivity pattern aligned with the streamwise direction. The seabed fixity suppresses rigid-body motion, concentrating dynamic energy into elastic deformation. At higher frequencies, drivetrain-induced excitations generate a more axisymmetric radiation pattern, as shaft and gear-mesh loads are torsional and distributed rather than associated with a single translational mode. The shallow-water environment ($H = 30$ m) further constrains vertical propagation, sustaining acoustic energy over longer horizontal distances and promoting a quasi-2D spreading regime.

From an environmental perspective, the spectral overlap with marine fauna hearing ranges (Section 3) indicates that the signal is detectable at short distances, particularly in the mid- to high-frequency bands. However, audibility does not imply physiological impact [25], and rapid geometric spreading significantly limits the biologically relevant spatial extent. Mitigation strategies targeting the two dominant source mechanisms — vibration isolation of the nacelle–drivetrain assembly and structural tuning of the monopile — could effectively reduce the underwater acoustic footprint.

Regarding model limitations, the structural response is obtained under steady operating conditions, and the drivetrain is represented by a synthetic excitation model, introducing uncertainty in absolute high-frequency amplitudes. On the acoustic side, the constant seabed reflection coefficient, homogeneous medium assumption, and image-method restriction to horizontally stratified domains omit range-dependent and bathymetric effects. Future work should pursue experimental validation against field measurements, incorporation of realistic metocean conditions, and extension to multi-turbine configurations for cumulative impact assessment.

5. Conclusions

- A physics-based vibroacoustic framework coupling aeroelastic simulations with an equivalent dipole acoustic model has been developed, providing a computationally efficient tool for structure-borne underwater noise assessment during the design phase.
- The acoustic response is frequency-dependent: global bending modes dominate at low frequencies, producing a streamwise-aligned dipolar pattern, while drivetrain excitations yield a nearly axisymmetric radiation at mid-to-high frequencies.
- Shallow-water confinement ($H = 30$ m) and the line-like monopile geometry promote cylindrical-like spreading (-10 dB/decade), sustaining acoustic energy over larger horizontal distances than in unbounded environments.
- Spectral overlap with marine fauna hearing ranges is observed at short distances, though its biological relevance must be interpreted in the context of rapid propagation decay and ambient masking.

Acknowledgments

This research has received funding from the European Union (ERC, Off-coustics, project number 101086075). However, the views and opinions expressed are those of the authors alone and do not necessarily reflect those of the European Union or the European Research Council. Neither the European Union nor the granting authority can be held responsible for them.

All authors gratefully acknowledge the Universidad Politécnica de Madrid (www.upm.es) for providing computing resources on Magerit Supercomputer and the computer resources at MareNostrum and the technical support provided by Barcelona Supercomputing Center (projects RES-IM-2024-1-0003 and RES-IM-2025-1-0011).

References

[1] J. A. Hildebrand, "Anthropogenic and natural sources of ambient noise in the ocean," *Marine Ecology Progress Series*, vol. 395, pp. 5–20, 2009. DOI: 10.3354/meps08353.

[2] H. Slabbekoorn, N. Bouton, I. van Opzeeland, A. Coers, C. ten Cate, and A. N. Popper, "A noisy spring: The impact of globally rising underwater sound levels on fish," *Trends in Ecology & Evolution*, vol. 25, no. 7, pp. 419–427, 2010. DOI: 10.1016/j.tree.2010.04.005.

[3] J. Tougaard, L. Hermannsen, and P. T. Madsen, "How loud is the underwater noise from operating offshore wind turbines?" *The Journal of the Acoustical Society of America*, vol. 148, no. 5, pp. 2885–2893, 2020. DOI: 10.1121/10.0002453.

[4] J. Jonkman, "Dynamics modeling and loads analysis of an offshore floating wind turbine," National Renewable Energy Laboratory (NREL), Tech. Rep. NREL/TP-500-41958, 2009.

[5] L. B. Bolívar, O. A. M. Sáchez, M. de Frutos, and E. Ferrer, *On the prediction of underwater aerodynamic noise of offshore wind turbines*, 2025. arXiv: 2501.12404 [physics.ao-ph]. [Online]. Available: https://arxiv.org/abs/2501.12404.

[6] C. Bak et al., "Description of the dtu 10 mw reference wind turbine," DTU Wind Energy, Denmark, Tech. Rep. DTU Wind Energy Report-I-0092, Jul. 2013.

[7] National Renewable Energy Laboratory (NREL), *Openfast: Wind turbine simulation code*, https://openfast.readthedocs.io/en/main/, Aug 2025.

[8] E. Branlard et al., "Superelement reduction of substructures for sequential load calculations in openfast," *Journal of Physics: Conference Series*, vol. 1452, p. 012 033, 2020, Open Access Paper.

[9] K. Betke, M. S.-v. Glahn, and R. Matuschek, "Underwater noise emissions from offshore wind turbines," ITAP – Institut für technische und angewandte Physik GmbH, Oldenburg, Germany, Technical Report, 2004.

[10] H. Lindell, "Utgrunden offshore wind farm - measurements of underwater noise," n.d., Technical Report, Jan. 2003.

[11] Y. G. Yoon, D.-G. Han, and J. W. Choi, "Measurements of underwater operational noise caused by offshore wind turbine off the southwest coast of korea," *Frontiers in Marine Science*, Jul. 2023. DOI: 10.3389/fmars.2023.1153843.

[12] Odegaard & Dannesjiold-Samsoe A/S, "Offshore wind turbines - vvm: Underwater noise measurements, analysis and predictions," SEAS Distribution A.m.b.A, Denmark, Tech. Rep. Report no. 00.729 rev.1, ODS ref 99.1314, Mar. 2020.

[13] M. J. Lighthill, "On sound generated aerodynamically i. general theory," *Proceedings of the Royal Society of London. Series A. Mathematical and Physical Sciences*, vol. 211, no. 1107, pp. 564–587, 1952. DOI: 10.1098/rspa.1952.0060.

[14] M. C. Junger and D. Feit, *Sound, Structures, and Their Interaction*, 2nd. Cambridge, MA: MIT Press, 1986.

[15] P. M. Morse and K. U. Ingard, *Theoretical Acoustics* (International Series in Pure and Applied Physics). New York: McGraw-Hill, 1968.

[16] E. L. Hamilton, "Geoacoustic modeling of the sea floor," *The Journal of the Acoustical Society of America*, vol. 68, no. 5, pp. 1313–1340, 1980, ISSN: 0001-4966. DOI: 10.1121/1.385100.

[17] S. Wang, A. R. Nejad, and T. Moan, "Design and dynamic analysis of a compact 10 mw medium speed gearbox for offshore wind turbines," *Journal of Offshore Mechanics and Arctic Engineering*, vol. 143, no. 3, Nov. 2020, ISSN: 1528-896X. DOI: 10.1115/1.4048608. [Online]. Available: http://dx.doi.org/10.1115/1.4048608.

[18] J. L. M. Peeters, D. Vandepitte, and P. Sas, "Analysis of internal drive train dynamics in a wind turbine," *Wind Energy*, vol. 9, no. 1-2, pp. 141–161, 2006. DOI: 10.1002/we.173. [Online]. Available: https://doi.org/10.1002/we.173.

[19] A. R. Nejad, E. E. Bachynski, L. Li, and T. Moan, "Correlation between acceleration and drivetrain load effects for monopile offshore wind turbines," *Energy Procedia*, vol. 94, pp. 487–496, 2016. DOI: 10.1016/j.egypro.2016.09.219. [Online]. Available: https://doi.org/10.1016/j.egypro.2016.09.219.

[20] Y. Guo, J. Keller, and W. LaCava, "Combined effects of gravity, bending moment, bearing clearance, and input torque on wind turbine planetary gear load sharing," National Renewable Energy Laboratory (NREL), Golden, CO, Tech. Rep. NREL/CP-5000-55968, 2012, Presented at the American Gear Manufacturers Association Fall Technical Meeting, 2012.

[21] D. J. Inman, *Engineering Vibration*, Fourth. Boston, MA: Pearson, 2014, ISBN: 9780132871693.

[22] S. Wang, A. R. Nejad, and T. Moan, "On design, modelling, and analysis of a 10-mw medium-speed drivetrain for offshore wind turbines," *Wind Energy*, vol. 23, no. 4, pp. 1099–1117, 2020, Received: 16 April 2019; Revised: 8 December 2019; Accepted: 15 December 2019, ISSN: 1099-1824. DOI: 10.1002/we.2476.

[23] A. Sehgal, I. Tumar, and J. Schönwälder, "Variability of available capacity due to the effects of depth and temperature in the underwater acoustic communication channel," in *Proceedings of IEEE OCEANS 2010*, IEEE, Jun. 2009.

[24] International Organization for Standardization, *Iso 266: Acoustics — preferred frequencies*, 1997.

[25] B. L. Southall et al., "Marine mammal noise exposure criteria: Updated scientific recommendations for residual hearing effects," *Aquatic Mammals*, vol. 45, no. 2, pp. 125–232, 2019. DOI: 10.1578/AM.45.2.2019.125.

[26] J. Tougaard, "Thresholds for noise-induced hearing loss in marine mammals," Aarhus University, DCE - Danish Centre for Environment and Energy, Tech. Rep. Scientific Note No. 2021—28, 2021. [Online]. Available: https://dce.au.dk/fileadmin/dce.au.dk/Udgivelser/Notater_2021/N2021_28.pdf.

[27] National Marine Fisheries Service, "Technical guidance for assessing the effects of anthropogenic sound on marine mammal hearing (version 2.0)," National Oceanic and Atmospheric Administration (NOAA), Tech. Rep. NMFS-OPR-59, 2024.

[28] C. Erbe, C. Reichmuth, K. Cunningham, K. Lucke, and R. Dooling, "Communication masking in marine mammals: A review and research strategy," *Marine Pollution Bulletin*, vol. 103, no. 1-2, pp. 15–38, 2016. DOI: 10.1016/j.marpolbul.2015.12.007.

[29] A. Kahraman, "Load sharing characteristics of planetary transmissions," *Mechanism and Machine Theory*, vol. 29, no. 8, pp. 1151–1165, 1994, ISSN: 0094-114X.

[30] Q. Ge, H. Yao, S. Qian, X. Zhang, and H. Guo, "Dependencies of underwater noise from offshore wind farms on distance, wind speed, and turbine power," *Acoustics*, vol. 7, no. 4, p. 71, 2025. DOI: 10.3390/acoustics7040071. [Online]. Available: https://doi.org/10.3390/acoustics7040071.